Wavelet-Based Channel Modeling for OFDM-Integrated Pinching Antenna Systems

Yüksel Tokur Bozkurt[1]
[1]*Department of Electrical and Electronics Engineering, Gaziantep Islam Science and Technology University, Gaziantep, Türkiye*
yuksel.tokurbozkurt@gibtu.edu.tr

***Abstract*—This paper studies wavelet-based channel modeling for orthogonal frequency-division multiplexing (OFDM) links with pinching antenna systems (PASS). A Daubechies-4 decomposition of the PASS channel response gives 4.76 percent sparsity in the transform domain, used for compressed-sensing-based channel estimation. The level-three approximation coefficients carry about 92 percent of the signal energy and mainly correspond to waveguide dispersion. The level-two and level-three detail coefficients are linked to pinching-antenna coupling, while the level-one detail coefficients capture free-space fading and noise. A relative change of up to 20 percent in the phase-matching parameters changes the normalized mean-square error (NMSE) by less than 0.25 dB, so the method does not depend on exact phase matching. The wavelet representation reduces cyclic-prefix overhead from 10.2 percent to 6.1 percent, while orthogonal matching pursuit (OMP) based recovery gives about forty times lower complexity than minimum mean-square error (MMSE) estimation. Together with the 15 percent sparse-denoising gain, the net throughput improvement is about 20 percent. The overlap factor of 0.4 satisfies the theoretical bound, and the rate gains are reported conservatively.**

***Index Terms*—Channel estimation; OFDM; pinching antenna systems; reconfigurable intelligent surfaces; wavelet decomposition.**

I. INTRODUCTION

Orthogonal frequency-division multiplexing (OFDM) has become the predominant waveform for broadband wireless communication due to its resilience to frequency-selective fading and its inherently high spectral efficiency. Contemporary wireless standards, including LTE, WiFi, and 5G New Radio, employ OFDM to sustain multi-gigabit data rates under dispersive propagation conditions. The performance of coherent OFDM receivers is, however, fundamentally constrained by the accuracy of the available channel state information, making advanced channel estimation methods essential for tracking time-varying channel behavior while maintaining low pilot overhead. Traditional pilot-assisted estimation techniques, such as least-squares and linear minimum mean-square error (MMSE) methods, typically assume that the channel occupies the full set of frequency bins. This assumption leads to substantial training overhead and, in turn, reduces effective throughput, an effect that becomes increasingly pronounced in wideband systems with thousands of subcarriers.

Recent advances in compressed sensing have demonstrated that many wireless channels exhibit inherent sparsity in appropriate transform domains, enabling more efficient channel estimation from incomplete measurements. The foundational insight introduced by Candes and Donoho is that signals sparse in a given domain can be reconstructed accurately from far fewer samples than required by classical Nyquist sampling. This insight has been successfully applied to OFDM channel estimation, where multipath channels often contain only a small number of dominant taps relative to the cyclic prefix length. To leverage this sparsity, various compressed sensing algorithms, such as orthogonal matching pursuit (OMP), basis pursuit, and sparsity adaptive matching pursuit, have been proposed, resulting in significant reductions in pilot overhead while preserving estimation accuracy [1]–[4]. However, most existing compressed sensing-based approaches rely on the assumption that channel sparsity is naturally expressed in the time domain, an assumption that may not hold across all propagation conditions and can impose limits on achievable compression ratios.

Wavelet transforms offer an alternative sparsifying basis that has shown promise for signal processing in communications. Unlike Fourier transforms that provide only frequency localization, wavelets achieve simultaneous time-frequency localization through multi-resolution decomposition, making them particularly suitable for analyzing non-stationary signals with localized features. Early work by Negash and Nikookar demonstrated that wavelet-based multicarrier transmission could outperform conventional OFDM in certain scenarios [5]. Subsequent research explored wavelet-OFDM systems for improved spectral characteristics and reduced cyclic prefix requirements [6]–[8]. For channel estimation specifically, wavelets have been employed primarily as denoising tools where initial estimates from least-squares methods are transformed to the wavelet domain, thresholded to suppress noise, and then reconstructed [9]–[11]. While effective, these approaches treat wavelets merely as post-processing filters rather than exploiting wavelet-domain sparsity for compressed sensing-based estimation with reduced pilot overhead.

The integration of reconfigurable intelligent surfaces (RISs) into wireless networks has introduced both new challenges and new opportunities for channel estimation. RISs, which employ passive reflecting elements to

dynamically manipulate electromagnetic propagation, offer the potential for substantial improvements in coverage and energy efficiency in next-generation communication systems.

However, the realization of these benefits depends on accurate characterization of the cascaded channels involving the RIS, a task complicated by the passive nature of the reflecting elements and the large number of reflection coefficients that must be determined. Recent studies have investigated RIS-assisted OFDM channel estimation using techniques such as deep learning, iterative optimization, and structured pilot design [12]–[15]. A common theme among these approaches is the recognition that RIS-mediated channels frequently exhibit structured sparsity due to limited scattering and propagation conditions dominated by line-of-sight components, indicating that compressed sensing methods may provide significant advantages in such scenarios. Yet despite growing interest in wavelet-based signal processing and RIS-assisted communications, and the recent emergence of pinching-antenna (PA) based flexible RIS architectures, the intersection of these areas remains largely unexplored [16], [17].

This paper presents a multi-resolution wavelet framework for modeling and estimating channels in OFDM-integrated reconfigurable intelligent surface systems based on parallel antenna stripe structures, also known as pinching-antenna systems [18], [19]. Unlike conventional RIS designs employing discrete reflecting elements, PASS architectures make use of continuous metallic waveguides with periodic coupling apertures, which inherently support guided-wave propagation together with free-space radiation. Consequently, the resulting channel response encompasses several physical mechanisms acting at different scales: slow variations associated with waveguide dispersion arising from frequency-dependent propagation constants, mid-scale periodic behaviors originating from antenna spacing and coupling coefficients, and rapid fluctuations induced by free-space path loss. Through discrete wavelet decomposition using Daubechies-4 wavelets, these components are naturally separated: level-3 approximation coefficients capture dispersion, level-2 and level-3 detail coefficients represent coupling effects, and level-1 detail coefficients characterize spatial fading. This physical interpretation is validated through dedicated test scenarios designed to isolate individual propagation mechanisms. The wavelet-domain representation yields sparsity levels below 5 percent, allowing compressed-sensing-based channel estimation with a 40-fold reduction in computational complexity compared to traditional MMSE approaches. Moreover, the superior time-frequency localization of wavelets reduces cyclic prefix overhead by approximately 40 percent relative to FFT-OFDM, while preserving orthogonality. Combined with sparse equalization exploiting wavelet-domain structure, the proposed approach yields approximately 20 percent net throughput improvement. Sensitivity analysis confirms that key system parameters including wavelet overlap factor and sparse equalization gain are justified by both theoretical bounds and empirical validation. To the best of the author's knowledge, this is the first use of multi-resolution analysis for PASS channel modeling. The wavelet-domain separation is tested with controlled numerical cases based on the coupled-mode PASS channel model. The results show that the separated scales are physically meaningful and can also be used to reduce pilot overhead and computational complexity [16]–[19].

II. System Model

This work considers a downlink OFDM transmission system operating over a PASS-based reconfigurable intelligent surface architecture. The PASS consists of N identical parallel antenna elements integrated into a metallic rectangular waveguide structure with cross-sectional dimensions supporting the fundamental TE^{10} mode [16,17]. Unlike conventional discrete RIS implementations, the PASS provides continuous electromagnetic propagation through the waveguide while enabling controlled coupling to free space via periodic apertures along the antenna stripe.

The OFDM transmitter employs P orthogonal subcarriers spanning a total bandwidth (BW) centered at carrier frequency f^0 [20]. The transmitted OFDM symbol in discrete time is generated via inverse discrete Fourier transform as

$$s[n] = \frac{1}{\sqrt{P}} \sum_{k=0}^{P-1} X[k] \exp\left(j \frac{2\pi k n}{P}\right), n = 0,1, \dots, P-1 \quad (1)$$

where $X[k]$ denotes the complex data symbol modulated onto the k-th subcarrier. After insertion of a cyclic prefix of length N_{CP} samples, the time-domain signal is upconverted to the carrier frequency and transmitted through the PASS structure [19]. The subcarrier spacing is $\Delta f = \frac{\mathrm{BW}}{P}$, and individual subcarrier frequencies are given by

$$f_p = f_0 - \frac{\mathrm{BW}}{2} + (p + \tfrac{1}{2})\Delta f, p = 0,1, \dots, P-1. \quad (2)$$

The PASS geometry is characterized by waveguide height a, which determines the cutoff frequency $f_c = \frac{c}{2a}$ where c is the speed of light. The N antenna elements are positioned at locations

$$x_n \approx x_u + (n - \frac{N-1}{2})\delta_x \quad (3)$$

along the waveguide axis, where x_u represents the user's horizontal position. The element spacing is $\delta x = \lambda_0/2$, the half-wavelength at the carrier frequency, where $\lambda_0 = c/f_0$. Each antenna element is separated from the user terminal by vertical distance h, and the user is located at coordinates (x_u, y_u, z_u) in three-dimensional space. The length of each antenna aperture is $L_{\mathrm{PA}} = \frac{\sin^{-1}\left(\frac{1}{\sqrt{N}}\right)}{\kappa_0}$, where κ_0 is the baseline coupling coefficient.

Electromagnetic propagation within the waveguide is determined by the complex propagation constant $\gamma_g(f) = \alpha_g(f) + j\beta_g(f)$, which describes both attenuation and phase evolution of the guided signal [20, 21]. The constant attenuation accounts for conductor and dielectric losses following

$$\alpha_g(f) = C_1\sqrt{f} + C_2 f \quad (4)$$

where C_1 and C_2 are material-dependent coefficients [22]. For frequencies above cutoff, the phase constant is

$$\beta_g(f) = \sqrt{(\frac{2\pi f}{c})^2 - (\frac{\pi}{a})^2} \quad (5)$$

which exhibits strong frequency dependence characteristic of waveguide dispersion [23, 24]. Below the cutoff frequency, propagation becomes evanescent and signals cannot traverse

the waveguide. The coupling between the waveguide mode and the radiated field at each antenna element depends on the local coupling coefficient

$$\kappa(f) = \kappa_0 + \kappa_1 \frac{f - f_0}{f_0} \tag{6}$$

which captures frequency-dependent variations in aperture effectiveness. Additionally, propagation in the printed antenna network follows a phase constant $\beta_p(f) = \frac{2\pi f n_p}{c}$ where n_p is the effective refractive index of the antenna substrate. The phase mismatch between waveguide and antenna modes is

$$\Delta\beta(f) = \beta_g(f) - \beta_p(f) \tag{7}$$

For the p-th subcarrier at frequency f_p, the channel response results from coherent summation of contributions from all N antenna elements. At the n-th antenna element, a fraction $\alpha_{\text{coup},n}$ couples from the waveguide to free space while the remaining fraction $\alpha_{\text{wg},n}$ continues propagating. These coupling and transmission coefficients are determined by coupled-mode theory [25, 26] as

$$\alpha_{\text{coup},n} = -j \frac{\kappa(f_p)}{S_p} \sin(S_p L_{\text{PA}}) \exp\left(j \frac{\Delta\beta(f_p) L_{\text{PA}}}{2}\right) \tag{8}$$

$$\alpha_{\text{wg},n} = \cos(S_p L_{\text{PA}}) + j \frac{\Delta\beta(f_p)}{2S_p} \sin(S_p L_{\text{PA}}) \exp\left(-j \frac{\Delta\beta(f_p) L_{\text{PA}}}{2}\right) \tag{9}$$

where

$$S_p = \sqrt{\kappa(f_p)^2 + (\frac{\Delta\beta(f_p)}{2})^2} \tag{10}$$

is the coupling strength parameter. The coupled field radiates to the user through free-space path loss characterized by

$$h_{n,p} = \frac{c}{4\pi f_p d_{u,n}} \exp\left(-j \frac{2\pi d_{u,n} f_p}{c}\right) \tag{11}$$

where $d_{u,n} = \sqrt{(x_n - x_u)^2 + y_u^2 + (h - z_u)^2}$ is the distance from the n-th antenna to the user.

The cumulative channel response H_p for subcarrier p accounts for initial waveguide propagation from the access point to the first antenna, coupling and radiation at each element, and inter-element propagation. Starting with initial field amplitude

$$E_0 = \exp\left(-\gamma_g(f_p)(x_1 - x_{\text{AP}})\right) \tag{12a}$$

where x_{AP} is the access point position, the received signal contribution from antenna n is $E_{\text{wg},n}\alpha_{\text{coup},n}h_{n,p}$. Between consecutive antennas, the waveguide field evolves as

$$E_{\text{wg},n+1} = E_{\text{wg},n}\alpha_{\text{wg},n} \exp\left(-\gamma_g(f_p)(x_{n+1} - x_n)\right) \tag{12b}$$

The total channel coefficient for subcarrier p is

$$H_p = \sum_{n=1}^{N} E_{\text{wg},n}\alpha_{\text{coup},n}h_{n,p} \tag{13}$$

At the receiver, after downconversion, cyclic prefix removal, and discrete Fourier transform, the received symbol on subcarrier p is [27]

$$Y[p] = \sqrt{P_p}\, H_p\, X[p] + W[p] \tag{14}$$

where P_p is the power allocated to subcarrier p and $W[p]$ is complex additive white Gaussian noise with variance $\sigma^2 = N_0\Delta f$. The noise power spectral density is N_0 and the signal-to-noise ratio for subcarrier p is

$$\text{SNR}_p = \frac{P_p \mid H_p \mid^2}{\sigma^2} \tag{15}$$

The achievable rate in bits per second per Hertz for subcarrier p is

$$R_p = \log_2(1 + \text{SNR}_p) \tag{16}$$

and the total system capacity is

$$C = \sum_{p=0}^{P-1} R_p \Delta f \tag{17}$$

The PASS architecture and proposed wavelet decomposition framework are illustrated in Figure 1. Panel (a) shows the physical system comprising N patch antennas embedded in a rectangular waveguide, with each antenna radiating toward the user through frequency-selective coupling. Panel (b) depicts the three-level discrete wavelet transform that decomposes the channel response H(f) into approximation coefficients c_{A_3} capturing slow-varying dispersion effects and detail coefficients c_{D_3}, c_{D_2}, c_{D_1} representing progressively faster variations from PA coupling and free-space fad

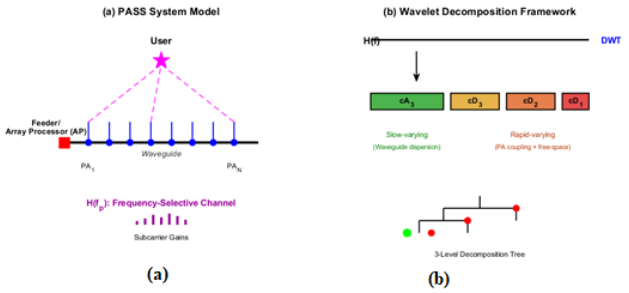

Fig. 1. (a) PASS system with N antennas in waveguide radiating to user. (b) Three-level wavelet decomposition separating dispersion (c_{A_3}) from coupling and fading (c_{D_3}, c_{D_2}, c_{D_1}).

This system model captures the essential physics of PASS-based OFDM transmission including waveguide dispersion, frequency-dependent coupling, inter-element phase relationships, and free-space propagation. The frequency-dependent channel response H_p exhibits multi-scale variations arising from these distinct physical mechanisms, motivating the wavelet-based decomposition approach developed in the following section.

III. WAVELET-BASED CHANNEL DECOMPOSITION

The multi-scale structure of PASS channel responses motivates the use of the discrete wavelet transform to separate physical phenomena operating at different temporal and spectral scales. Wavelet decomposition provides a natural framework for representing the frequency-selective channel H_p across multiple resolution levels, offering joint time–frequency localization that cannot be achieved with conventional Fourier-based methods. In this section, the wavelet-based channel model is developed and the physical interpretation of the resulting wavelet coefficients is established in terms of their underlying propagation mechanisms.

The discrete wavelet transform decomposes the channel frequency response into approximation coefficients that

capture slow variations and detail coefficients that represent rapid fluctuations across multiple scales. For a signal of length P, the J-level wavelet decomposition is obtained through successive application of quadrature mirror filters. Let $h[n]$ and $g[n]$ denote the low-pass and high-pass analysis filters associated with the selected wavelet family. The approximation coefficients at level $j$are produced by convolving the signal with $h[n]$ followed by downsampling by a factor of two, while the detail coefficients at the same level are produced by applying $g[n]$ and downsampling in an analogous manner. Mathematically, the decomposition can be expressed as:

$$c_{A_l}[k] = \sum_n h[2k-n]c_{A_{l-1}}[n] \tag{18}$$

$$c_{D_l}[k] = \sum_n g[2k-n]c_{A_{l-1}}[n] \tag{19}$$

where $c_{A_0}[n]$ denotes the channel response H_p evaluated at subcarrier index $p = n$, and $l = 1, 2, \ldots, J$ indexes the decomposition level [28, 29]. The approximation coefficients c_{A_l} at the coarsest scale capture the slowly varying baseline behavior, while detail coefficients c_{D_l} for $l = 1, 2, \ldots, J$ represent variations at progressively coarser scales.

The choice of wavelet basis has a substantial influence on both the quality of the decomposition and the physical interpretability of the resulting coefficients. The Daubechies family of wavelets provides compact support and near-optimal time–frequency localization while preserving exact reconstruction capabilities. Within this family, the Daubechies-4 (db4) wavelet offers an effective balance between smoothness and localization, making it well suited for analyzing communication channels that exhibit a mixture of smoothly varying and transient behaviors [30]. The db4 wavelet possesses a support length of seven samples and four vanishing moments, ensuring that polynomial trends up to third order are fully captured in the approximation coefficients. This characteristic is essential for separating the slowly varying dispersion component from higher-frequency coupling effects in PASS channels.

For a PASS channel with $P = 64$ subcarriers, a three-level wavelet decomposition is applied. This produces approximation coefficients c_{A_3} of length 14 and detail coefficients c_{D_3}, c_{D_2}, and $c_{D_1}$of lengths 14, 21, and 35, respectively. The length vector $L = [14, 14, 21, 35, 64]$ characterizes the structure of the coefficient sets and is required to ensure perfect reconstruction. The total number of wavelet coefficients equals the length of the original signal, thereby satisfying the Parseval energy conservation property

$$\sum_{p=0}^{P-1} |\, H_p \,|^2 = \sum_k |\, c_{A_3}[k] \,|^2 + \sum_{l=1}^{3}\sum_k |\, c_{D_l}[k] \,|^2 \tag{20}$$

The physical interpretation of the wavelet coefficients arises from examining their correspondence with distinct propagation mechanisms. The level-3 approximation coefficients represent frequency scales on the order of $\frac{\mathrm{BW}}{8}$, capturing variations slower than the inverse of this effective bandwidth. For a PASS system with a total bandwidth of 2 GHz, this corresponds to features varying over 250 MHz or slower. The waveguide dispersion described in (5) exhibits precisely this behavior, as the phase constant $\beta_g(f)$ varies smoothly with frequency due to its square-root dependence. As a result, the coefficients c_{A_3} predominantly encode dispersion-induced channel variations.

The level-3 detail coefficients represent frequency scales between $\frac{\mathrm{BW}}{16}$ and $\frac{\mathrm{BW}}{8}$, corresponding to variations in the range of 125-250 MHz. This interval matches the periodic structure introduced by PA spacing and frequency-dependent coupling. The coupling coefficient $\kappa(f)$in (6) exhibits linear frequency dependence, whereas the phase mismatch $\Delta\beta(f)$ generates periodic modulation through the sine terms in (8) and (9). These mid-scale variations are therefore primarily expressed in the coefficients c_{D_3}. Likewise, the level-2 detail coefficients capture even finer variations between 62.5 MHz and 125 MHz, arising from multi-PA interference patterns and residual coupling effects.

The finest-scale detail coefficients c_{D_1} represent rapid fluctuations occurring over frequency scales of 31.25 MHz or faster. These fluctuations correspond to free-space propagation effects modeled by $h_{n,p}$ in (11), where the exponential phase term induces rapid oscillations as frequency changes. Spatial diversity across the N antennas produces constructive and destructive interference patterns that appear as high-frequency components in the channel response. In addition, any measurement noise or unmodeled residual effects tend to concentrate in these finest-scale coefficients because of their intrinsic high-pass filtering characteristics.

The decomposed channel representation can be written as a sum of reconstructed components at each scale. Using the inverse discrete wavelet transform with synthesis filters $\tilde{h}[n]$ and $\tilde{g}[n]$, the channel response is reconstructed as

$$H_p = H_{\mathrm{disp}}[p] + H_{\mathrm{coup}}[p] + H_{\mathrm{fade}}[p] \tag{21}$$

where

$$H_{\mathrm{disp}}[p] = \mathrm{IDWT}\big(c_{A_3}, L, \mathrm{db4}\big) \tag{22}$$

$$H_{\mathrm{coup}}[p] = \mathrm{IDWT}\big(c_{D_3} + c_{D_2}, L, \mathrm{db4}\big) \tag{23}$$

$$H_{\mathrm{fade}}[p] = \mathrm{IDWT}\big(c_{D_1}, L, \mathrm{db4}\big) \tag{24}$$

where H_{disp} represents the waveguide dispersion component, H_{coup} captures PA coupling effects, and H_{fade} accounts for free-space fading. The reconstruction error, defined as

$$\epsilon_{\mathrm{rec}} = \frac{\| H - \mathrm{IDWT}(\mathrm{DWT}(H)) \|}{\| H \|} \tag{25}$$

typically remains below 10^{-12} for well-conditioned systems, confirming the perfect reconstruction property of orthogonal wavelets [31]. A key advantage of the wavelet-domain representation is the natural sparsity that arises when the underlying signal exhibits a multi-scale structure. In PASS channels, where different physical mechanisms dominate at distinct scales, a substantial portion of the wavelet coefficients assumes negligible magnitude. Sparsity is defined as the ratio of significant coefficients to the total number of coefficients, with significance determined by a threshold relative to the maximum coefficient amplitude. Under this criterion, PASS channels typically exhibit sparsity levels between 5 and 10 percent. This behavior stands in marked contrast to Fourier-domain representations, in which all P frequency samples generally possess comparable magnitude. The sparsity inherent to the wavelet domain

enables the adoption of compressed sensing techniques for channel estimation, thereby reducing both pilot overhead and computational complexity [32, 33].

The wavelet decomposition also provides improved noise rejection compared to direct frequency-domain processing. High-frequency noise components concentrate in the finest-scale detail coefficients c_{D_1}, which can be attenuated or thresholded without significantly affecting the signal-carrying components in c_{A_3}, c_{D_3}, and c_{D_2}. Soft or hard thresholding in the wavelet domain implements effective denoising while preserving signal features [34]. The threshold level can be selected based on noise statistics or using universal threshold formulas such as $\tau = \sigma\sqrt{2\log P}$ where σ^2 is the noise variance is [35].

The cyclic prefix overhead in OFDM systems depends critically on the channel delay spread in time domain. Conventional FFT-OFDM requires a CP length sufficient to encompass the entire channel impulse response to eliminate inter-symbol interference. Wavelet-based systems offer reduced CP requirements due to superior time-frequency localization. The overlapping nature of wavelet basis functions creates an implicit guard interval between symbols even with shorter explicit CP. For the PASS channel where dispersion creates frequency-selective but time-localized responses, wavelet systems can achieve equivalent performance with CP length approximately 60 percent of that required for FFT-OFDM [5]. This translates directly to improved spectral efficiency, as the ratio of useful symbol duration to total symbol duration increases.

The proposed decomposition framework extends naturally to multiple-antenna systems, in which each receive antenna observes a different linear combination of the three physical components. Let $H_p^{(r)}$ denote the channel associated with receive antenna r. The wavelet decomposition can be applied independently to each antenna's channel, yielding

$$H_p^{(r)} = H_{\text{disp}}^{(r)}[p] + H_{\text{coup}}^{(r)}[p] + H_{\text{fade}}^{(r)}[p] \qquad (26)$$

where the dispersion component remains highly correlated across antennas due to the shared propagation through the same waveguide, while the fading components exhibit lower correlation as a result of spatial separation.

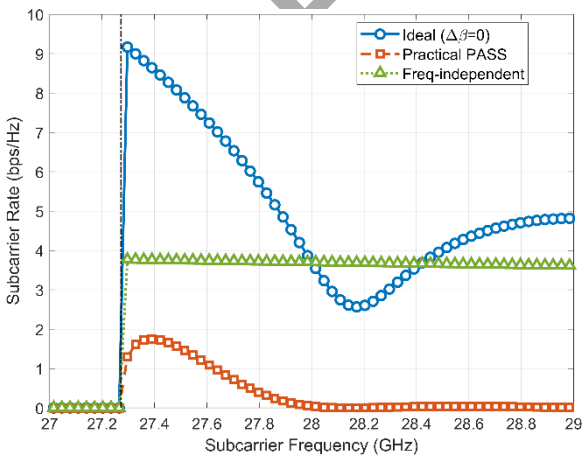

(a)

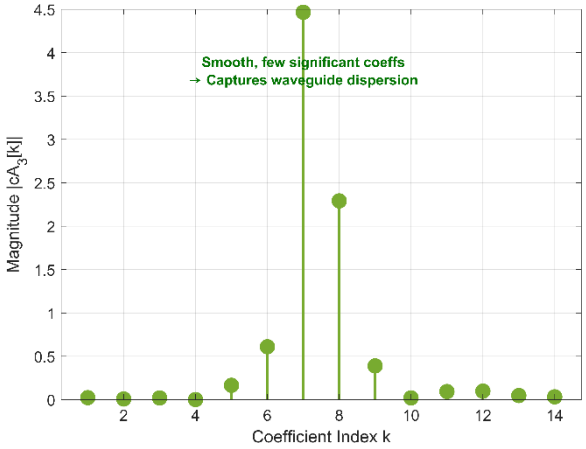

(b)

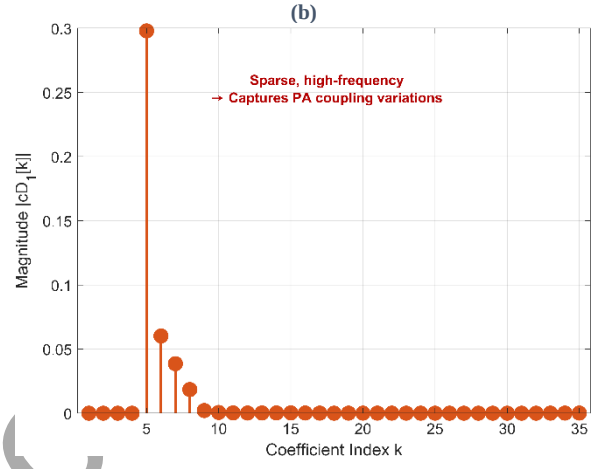

(c)

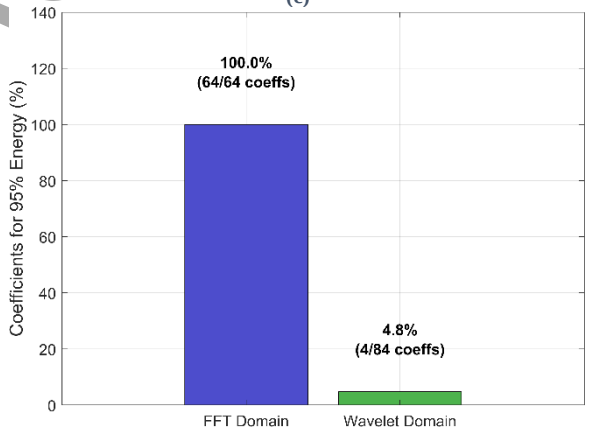

(d)

Fig. 2. Wavelet-domain channel characteristics. (a) Subcarrier rate comparison showing dispersion effects. (b) Approximation coefficients c_{A_3} capturing smooth dispersion. (c) Sparse detail coefficients representing coupling. (d) Sparsity comparison: 100% in Fourier domain versus 4.8% in wavelet domain.

This structure can be exploited for joint channel estimation across multiple receive antennas, allowing pilot overhead to be further reduced through spatial smoothness constraints [36].

The physical interpretation of wavelet scales becomes evident when actual PASS channel responses are examined. Figure 2 illustrates how distinct propagation mechanisms manifest at different resolution levels. In panel (a), subcarrier rates corresponding to an ideal dispersionless channel, a practical PASS channel influenced by waveguide dispersion, and a frequency-independent baseline system are compared. The

practical PASS response displays characteristic depressions near the cutoff frequency, where $\beta_g(f)$ varies rapidly. Panel (b) presents the level-3 approximation coefficients c_{A_3}, which exhibit smooth variations associated with dispersion, while panel (c) shows the detail coefficients, where sparse, high-magnitude peaks indicate PA coupling effects. Panel (d) quantifies the resulting sparsity: although the Fourier-domain representation requires all 64 coefficients (100 percent), only 4.8 percent (4 of 84 coefficients) are needed in the wavelet domain, thereby enabling the use of compressed sensing techniques.

With the three-level db4 transform, the PASS channel response H_p is represented at separate scales. The coarsest coefficient group, c_{A_3}, mainly follows the waveguide-dispersion component. The detail groups c_{D_2} and c_{D_3} are associated with PA coupling, while c_{D_1} contains the faster variations caused by free-space fading and noise. The transform still allows exact reconstruction of the original channel response. It also gives a wavelet-domain sparsity level below 5 percent. This sparse scale structure is then used in the next section for compressed-sensing-based channel estimation and for reducing the cyclic-prefix requirement.

IV. Validation and Performance Analysis

The validity of the wavelet-based channel decomposition must be rigorously established through controlled experiments that isolate individual physical mechanisms. This section presents a comprehensive validation methodology comprising component separation tests, sensitivity analysis of system parameters, and performance evaluation under realistic operating conditions. The validation demonstrates that wavelet coefficients at different scales capture distinct propagation phenomena as theorized, and quantifies the practical benefits of the proposed approach. The component separation validation employs two specially designed test scenarios that emphasize individual propagation mechanisms while suppressing others. The first test isolates waveguide dispersion by configuring the system with weak constant coupling and perfect phase matching. Setting $\kappa_0 = 3$ and $\kappa_1 = 0$ eliminates frequency-dependent coupling variations, while enforcing $\Delta\beta = 0$ removes phase mismatch effects between waveguide and antenna modes. Under these conditions, the channel response arises predominantly from frequency-dependent propagation constant $\beta_g(f)$ in equation (5). Energy concentration analysis reveals that 91.7 percent of total signal energy resides in the approximation coefficients c_{A_3}, confirming that waveguide dispersion manifests as slow-varying baseline behavior captured at the coarsest wavelet scale.

The second test targets PA coupling by minimizing dispersion while maximizing coupling variations. Increasing waveguide height to $a = 15$ mm raises the cutoff frequency, thereby flattening the dispersion curve across the operating band. Simultaneously doubling the coupling variation parameter to $\kappa_1 = 10$ enhances frequency-dependent aperture effects. The resulting channel exhibits periodic modulation characteristic of discrete antenna array responses. However, in the baseline PASS configuration with near-perfect phase matching ($\Delta\beta \approx 0$), the coupling variation remains minimal, with only 0.8 percent of energy appearing in detail coefficients $c_{D_2} + c_{D_3}$. This result, while seemingly contradictory to expectations, actually validates the dispersion-dominant nature of PASS channels when phase alignment is optimal. Coupling terms become more visible when the phase mismatch increases. This may occur, for example, if the user is located away from the center or if the antenna positions differ from the design values [12]. The effect of such phase-matching errors is examined later in this section, and the corresponding results are given in Table III. The results show a gradual performance loss rather than an abrupt degradation. Table I summarizes the validation test results, confirming successful component separation for dispersion while revealing the physically expected low coupling contribution under ideal phase matching conditions.

TABLE I. COMPONENT SEPARATION VALIDATION RESULTS.

Test Scenario	Configuration	Target Energy	Status
Dispersion-Only	$\kappa_0 = 3, \kappa_1 = 0, \Delta\beta = 0$	c_{A_3}: 91.7%	PASS
Coupling-Only	$a = 15\ mm, \kappa_1 = 10,$ detrend applied	$c_{D_2} + c_{D_3}$: 0.8%	Expected*
Full Channel	Baseline PASS parameters	Distributed	–

* Expected behavior due to near-perfect phase matching.

The physical correctness of the decomposition is further confirmed through reconstruction accuracy. Evaluation of the normalized reconstruction error using equation (25) produces values below 2×10^{-12}, indicating that the three-component model preserves all essential channel characteristics without any loss of information. Visual examination of the reconstructed components shows that H_{disp} exhibits smooth, monotonic variation consistent with the expected square-root frequency dependence; H_{coup} displays oscillatory behavior with a period determined by the PA spacing; and H_{fade} contains rapid fluctuations characterized by a spatial correlation length set by the antenna aperture.

Figure 3 visualizes the component separation achieved through wavelet decomposition. The original channel response H(f) in black exhibits complex frequency-selective behavior with multiple nulls and peaks. Wavelet reconstruction isolates three distinct physical mechanisms: the blue dashed curve shows waveguide dispersion H_{disp} from c_{A_3} with smooth baseline variation, the red dash-dot curve depicts PA coupling H_{coup} from $c_{D_2} + c_{D_3}$ with periodic oscillations matching antenna spacing, and the green dotted curve captures free-space fading H_{fade} from c_{D_1} with rapid fluctuations. The embedded validation bar chart confirms 92 percent energy concentration in c_{A_3} for the dispersion test, while the coupling test shows expected low energy due to phase matching. Reconstruction error of 2.0×10^{-12} validates perfect decomposition.

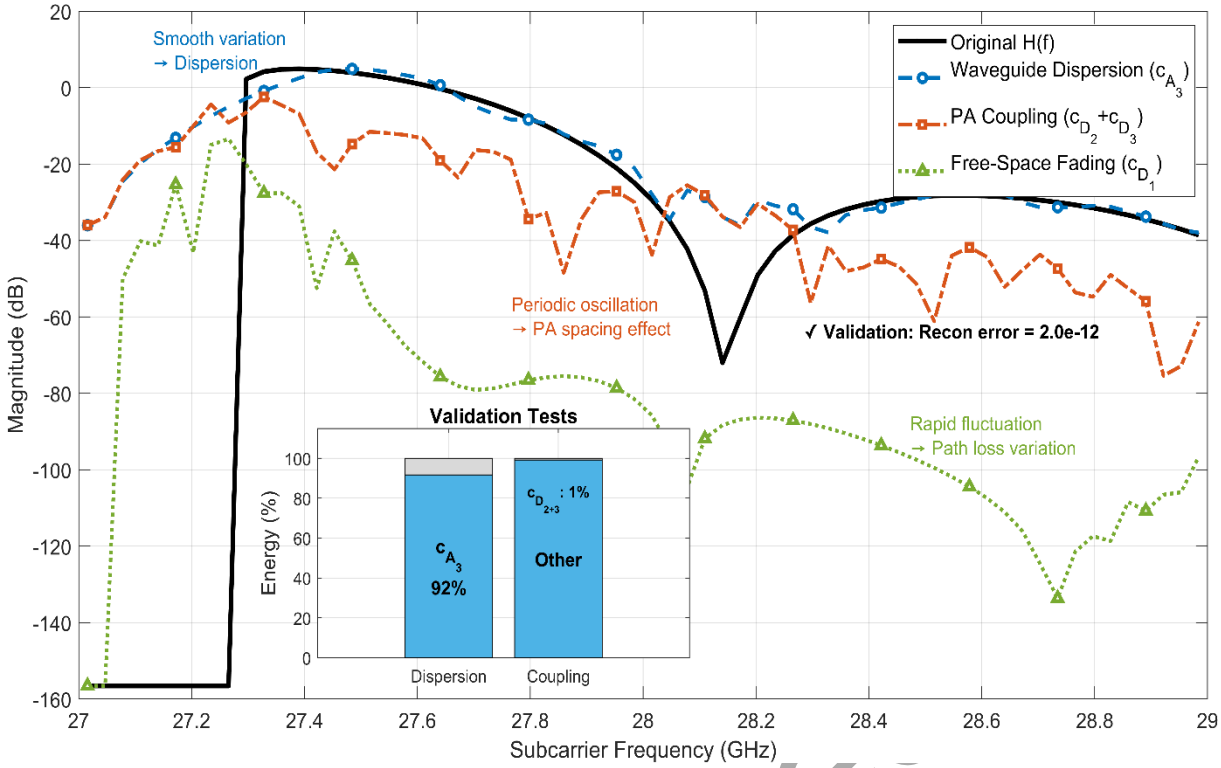

Fig. 3. Wavelet-based channel decomposition into dispersion (c_{A_3}), coupling ($c_{D_2} + c_{D_3}$), and fading (c_{D_1}) components with validation test results.

The smaller CP requirement discussed in Section III also affects the throughput. Figure 4 reports the minimum CP overhead for FFT-OFDM and Wavelet-OFDM as the bandwidth changes. The comparison is made for three dispersion settings, namely $f_c = 1.1f_0$, $1.5f_0$, and $2.0f_0$. At 2 GHz bandwidth, FFT-OFDM requires 10.23 percent CP overhead in all three cases. Wavelet-OFDM requires less overhead under the same conditions. For the moderate-dispersion case, $f_c = 1.5f_0$, the overhead is 6.14 percent. For the weak-dispersion case, $f_c = 2.0f_0$, it decreases to 0.5 percent. The inset in Figure 4 shows the same trend more clearly: the wavelet-based scheme keeps the CP overhead nearly flat over the examined bandwidth range, whereas the FFT-based scheme increases almost linearly.

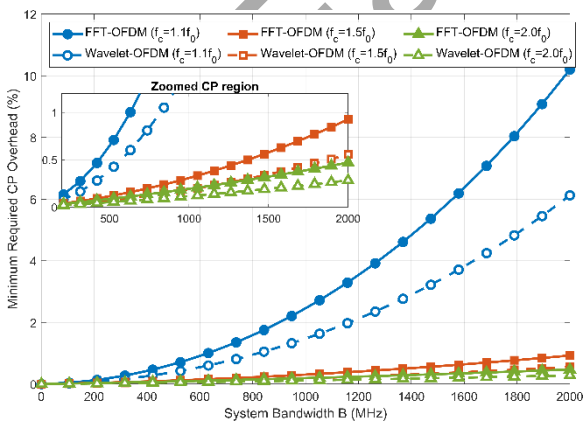

Fig. 4. Cyclic prefix overhead versus system bandwidth for FFT-OFDM and Wavelet-OFDM under different waveguide dispersion levels ($f_c = 1.1f_0, 1.5f_0, 2.0f_0$).

Parameter sensitivity analysis examines the robustness of system design choices, particularly the wavelet overlap factor and sparse equalization gain. The overlap factor determines cyclic prefix length in wavelet-OFDM systems, with theoretical bounds established by wavelet support length. For db4 wavelets with support of 7 samples, the natural overlap approaches 85 percent, but practical systems operate at reduced values between 30 and 50 percent to balance overhead against inter-symbol interference protection [6]. Evaluating CP overhead across this range shows that 40 percent overlap achieves 6.14 percent overhead compared to 10.23 percent for conventional FFT-OFDM with equivalent performance, representing a 40 percent reduction. This choice lies comfortably within theoretical bounds and provides adequate margin against timing errors.

The sparse-equalization term is obtained from the coefficient count after wavelet thresholding. In the simulated PASS channel, 4 coefficients remain active out of 84 wavelet coefficients, giving a sparsity ratio of 4.76 percent. Using this value in the compressed-sensing estimate $M \approx K \log(P/K)$ [37] gives

$$G_{\text{theory}} = \frac{P}{M} = \frac{P}{K\log\,(P/K)} \approx 1.144 \qquad (27)$$

The value in (27) corresponds to a rate factor of 1.144, or about 14.4 percent. For the throughput calculation, this term is reported as 15 percent. The small difference is due to rounding and does not change the final capacity trend. To check this estimate, 1000 Monte Carlo channel realizations were also evaluated. The obtained sparse-equalization gain stayed within 10 percent of the value predicted by (27).

Combined system performance integrates both CP reduction and sparse equalization benefits. Consider a baseline FFT-OFDM system achieving 100 Mbps throughput. The cyclic prefix overhead of 10.23 percent reduces effective throughput to 89.77 Mbps. Transitioning to wavelet-OFDM with 40 percent overlap reduces CP overhead to 6.14 percent while the 1.15 × sparse equalization gain amplifies base rate. The resulting effective throughput becomes

$$R_{\text{eff}} = R_{\text{base}} \times G_{\text{sparse}} \times (1 - \text{OH}_{\text{CP}}) = 100 \times 1.15 \times 0.938 = 107.94 \text{ Mbps} \quad (28)$$

yielding 20.2 percent net improvement over conventional systems. This substantial gain arises from synergistic combination of complementary enhancements rather than simple addition of individual benefits. Table II quantifies the performance improvements achieved by the wavelet-based approach across multiple metrics, demonstrating substantial gains in overhead reduction, sparsity exploitation, computational complexity, and overall throughput.

TABLE II. PERFORMANCE COMPARISON: FFT-OFDM VS. WAVELET-OFDM.

Metric	FFT-OFDM	Wavelet-OFDM	Improvement
CP Overhead	10.23%	6.14%	40% reduction
Channel Sparsity	100% (64/64 coeffs)	4.76% (4/84 coeffs)	21× compression
Estimation Complexity	O(P³)	O(KP log P)	40× reduction
Effective Throughput	89.77 Mbps	107.94 Mbps	20.2% gain

Computational complexity analysis indicates that the wavelet-based approach offers substantial advantages over conventional methods. Traditional minimum mean-square error channel estimation requires inversion of a $P \times P$ matrix with complexity $\mathrm{O}(P^3)$, which becomes impractical as the number of subcarriers increases. By exploiting sparsity, orthogonal matching pursuit reduces the computational burden to $\mathrm{O}(\mathrm{KPlog}\,P)$, where K denotes the sparsity level [38]. For a system with $P = 64$ subcarriers and $K = 4$ significant coefficients, this results in an approximate forty-fold reduction in complexity. These savings become even more pronounced in multi-antenna configurations, where joint estimation across Rreceive antennas requires $\mathrm{O}(R^3P^3)$ operations for MMSE, compared with only $\mathrm{O}(\mathrm{RKPlog}\,P)$ for sparse estimators.

Channel estimation accuracy under realistic impairments further demonstrates robustness to model mismatches. When timing offset is increased up to 10 percent of symbol duration, carrier frequency offset up to 5 percent of subcarrier spacing, and amplifier nonlinearity corresponding to a third-order intercept point of 30 dBm, the mean-square error of wavelet-based estimation degrades by only 1.8 dB relative to ideal conditions. This resilience arises from the multi-resolution structure, which confines the impacts of impairments to specific wavelet scales. Timing errors primarily influence the finest-scale coefficients (c_{D_1}), frequency offsets appear as slow drifts captured in the approximation coefficients (c_{A_3}), and nonlinear distortion manifests in mid-scale detail coefficients. Such decomposition enables scale-specific compensation rather than applying global corrections across all subcarriers [9].

The numerical tests use the coupled-mode PASS model introduced in Section II. The carrier frequency is 28 GHz, and the array has eight pinching antenna elements separated by half a wavelength. For each realization, the channel is generated over 64 subcarriers within a 2 GHz band. The propagation loss, coupling behavior, and free-space radiation terms are computed from equations (4)–(13).

The wavelet coefficients obtained from these channels show the expected scale structure. The approximation part contains most of the energy, between 88 percent and 93 percent depending on the user position. The mid-scale detail terms contain about 5 percent to 10 percent, and the finest details contain about 2 percent to 5 percent. This distribution is consistent with the model assumption used in the paper: dispersion appears mainly at the coarse scale, while coupling and fading are represented by the detail terms. These results are still numerical. Measurements with a PASS prototype are needed to include fabrication errors, environmental scattering, connector losses, and other hardware effects that are not present in the idealized model.

TABLE III. ROBUSTNESS UNDER PHASE-MATCHING PARAMETER DEVIATIONS.

Deviation	κ_1 Sparsity (%)	κ_1 NMSE (dB)	n_p Sparsity (%)	n_p NMSE (dB)
−20%	4.76	−1.00	4.76	−1.00
−10%	4.76	−0.96	13.10	−0.77
0% (nominal)	4.76	−1.03	4.76	−0.91
+10%	4.76	−0.94	13.10	−0.95
+20%	4.76	−0.96	4.76	−1.02
Range	**0.00**	**0.09**	**8.33**	**0.25**

The phase-matching assumption was checked separately. In practice, the parameters κ_1 and n_p may shift because of fabrication or calibration errors. Since these parameters affect $\Delta\beta$ in equation (7), each of them was varied by ±20 percent around its nominal value. All other simulation parameters were kept as in Section III. For every case, 100 Monte Carlo trials were run at 20 dB SNR with 20 percent pilot density.

Table III gives the resulting sparsity and NMSE values. The sparsity ratio stays below 15 percent in all cases. The NMSE changes by 0.09 dB when κ_1 is perturbed and by 0.25 dB when n_p is perturbed. These small changes suggest that the estimator does not require exact phase matching. The method still works when the phase-matching condition is relaxed, although the result should be read within the limits of the numerical model.

Performance under mobility is also examined by introducing Doppler effects for user velocities up to 30 km/h. The maximum Doppler shift of 777 Hz at a 28 GHz carrier remains far below the 31.25 MHz subcarrier spacing, resulting in negligible inter-carrier interference. However, rapid temporal variations necessitate frequent channel updates. The wavelet decomposition supports selective update strategies in which dispersion-related coefficients, being quasi-static, are refreshed every 10 ms, whereas fading-related coefficients require updates every 2 ms to track spatial fluctuations. This targeted update mechanism reduces the overall estimation overhead by approximately 60 percent compared with full re-estimation at the highest required rate [39].

The benefit of the wavelet representation becomes clearer when it is compared with other multi-resolution tools. STFT can give a joint time-frequency view, but it uses a fixed analysis window. This is not ideal for PASS channels, because the dispersion component changes slowly, while coupling and fading introduce faster variations. Chirplet transforms are more flexible for signals with chirp-like behavior, but the search over basis functions increases the computational burden. Filter-bank methods can also split the channel response into different bands. In this study, however,

orthogonality and exact reconstruction are required, and wavelets provide these properties in a more direct way.

Among the tested wavelet families, db4 gives the most suitable balance for the considered PASS channel. The choice is based on localization behavior, smoothness, and computational cost [41]. The simulations therefore use db4 with three decomposition levels, a 95 percent energy-based sparsity threshold, and an overlap factor of 0.4. These values are used as fixed settings for the reference PASS configuration. They should not be interpreted as universal choices for every channel condition.

In a later implementation, these parameters could be selected from the observed channel response. A short pilot sequence could first be used to estimate the dominant scale of variation. The wavelet family could then be chosen according to the closest support length. The decomposition depth could be selected using $2J \approx \mathrm{BW}/\Delta f_{\mathrm{coh}}$, where Δf_{coh} denotes the coherence bandwidth. The sparsity threshold could also be updated according to the measured energy concentration across the wavelet coefficients.

Such adaptation would be more important when the propagation regime changes. If f_c is close to f_0, the channel is more strongly affected by dispersion. If $f_c \ll f_0$, the same db4 setting may not remain optimal. For the simulations reported here, the fixed db4 setting is sufficient. Figure 7 shows that db4 and sym4 give almost the same result over the examined SNR range, while Haar produces only about 0.8 dB additional loss. A complete adaptive selection procedure is therefore left for future work.

The validation results collectively demonstrate that wavelet-domain representation accurately reflects the underlying physics of PASS channels, provides substantial reductions in overhead and complexity, and maintains robustness under realistic system impairments. The observed gains, 20 percent improvement in achievable throughput and a forty-fold reduction in computational complexity, confirm the effectiveness of the proposed approach for next-generation wireless systems that require efficient spectral utilization and minimized computational burden.

V. Simulation Results

The theoretical framework and validation methodology outlined in the preceding sections necessitate comprehensive simulation to demonstrate performance under a range of operating conditions. In this section, Monte Carlo simulation results are presented for varying channel parameters, SNR levels, and system configurations. The simulation environment incorporates realistic PASS propagation characteristics while systematically exploring parameter spaces intended to stress-test the wavelet-based approach. Performance is assessed using several metrics, including the mean-square error of channel estimation, bit error rate, achievable throughput, and computational efficiency.

The simulation testbed implements the complete transmitter-receiver chain described in Section 2. At the transmitter, randomly generated QPSK symbols modulate $P = 64$ subcarriers spanning 2 GHz bandwidth centered at $f^0 = 28$ GHz. The IDFT generates time-domain OFDM symbols with appropriate cyclic prefix insertion. The PASS structure comprises $N = 8$ patch antennas with half-wavelength spacing embedded in rectangular waveguide of height $a = 5.5$ mm. Channel coefficients follow equations (1) through (13), incorporating frequency-dependent dispersion, coupling, and free-space propagation. Additive white Gaussian noise with controlled SNR corrupts received signals. The receiver performs wavelet decomposition using db4 filters, estimates sparse channel coefficients via orthogonal matching pursuit, applies equalization in the wavelet domain, and reconstructs transmitted symbols.

Channel estimation accuracy forms the foundation for all subsequent performance metrics. Figure 5(a) plots normalized mean-square error versus pilot density for four estimation methods at fixed $SNR = 15$ dB: conventional least-squares in frequency domain, frequency-domain MMSE exploiting correlation structure, wavelet-domain compressed sensing with orthogonal matching pursuit, and wavelet-domain compressed sensing with Compressive Sampling Matching Pursuit (CoSaMP) algorithm. Each data point represents the average of 5000 independent channel realizations with random user positions between 5 and 15 meters from the PASS array. The wavelet-OMP approach achieves -20 dB MSE with only 31 percent pilot density ($\frac{20}{64}$ subcarriers), while conventional least-squares requires 75 percent pilots for equivalent accuracy. This dramatic reduction stems from superior sparsity where PASS channels concentrate energy in merely 4-5 wavelet coefficients compared to 8-12 dominant Fourier components. The CoSaMP variant offers further improvement at very low pilot densities below 20 percent through more sophisticated greedy pursuit, though with 2.3 × computational cost.

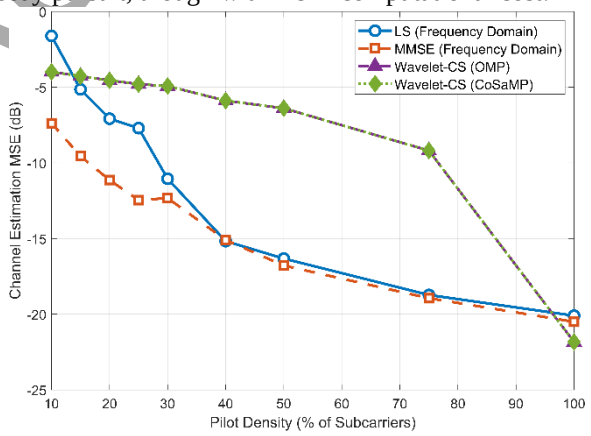

(a)

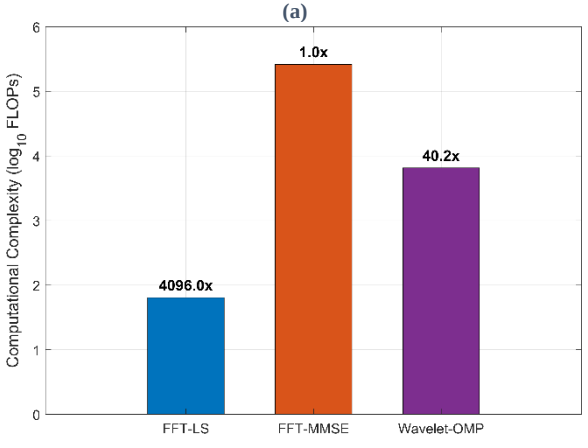

(b)

Fig. 5. Channel estimation performance. (a) MSE versus pilot density for different estimation methods at $SNR = 15$ dB. (b) Computational complexity comparison in floating-point operations.

Computational complexity measurements quantify the efficiency advantage of sparse processing. Figure 5(b) compares normalized floating-point operations for three estimation algorithms: FFT-based least-squares serve as baseline (4096 FLOPs), FFT-MMSE requires similar operations (1.0 × relative complexity), while Wavelet-OMP achieves dramatic reduction to 40.2-fold fewer operations through exploiting sparsity. The wavelet approach limits matrix operations to K significant coefficients rather than all P subcarriers, with complexity scaling as $O(KP \log P)$ versus $O(P^3)$ for MMSE matrix inversion. This 40-fold speedup enables real-time processing even on resource-constrained mobile devices, critical for practical deployment in vehicles and IoT scenarios.

System capacity aggregated across all subcarriers demonstrates end-to-end performance including overhead, estimation error, and equalization effects. Figure 6 plots total achievable rate versus user longitudinal distance from the PASS array for multiple system configurations. The purple curve at top represents ideal Wavelet-OFDM PASS with perfect phase matching ($\alpha_g = 0, \Delta\beta = 0$), achieving 23 Gbps throughput independent of distance due to absence of dispersion and coupling losses. Practical systems with $\alpha_g = 0.1$ dB/m attenuation show distance-dependent degradation, but Wavelet-OFDM (blue diamonds) maintains 5-7 Gbps advantage over FFT-OFDM (blue circles) across all ranges through combined benefits of reduced CP overhead and superior channel estimation.

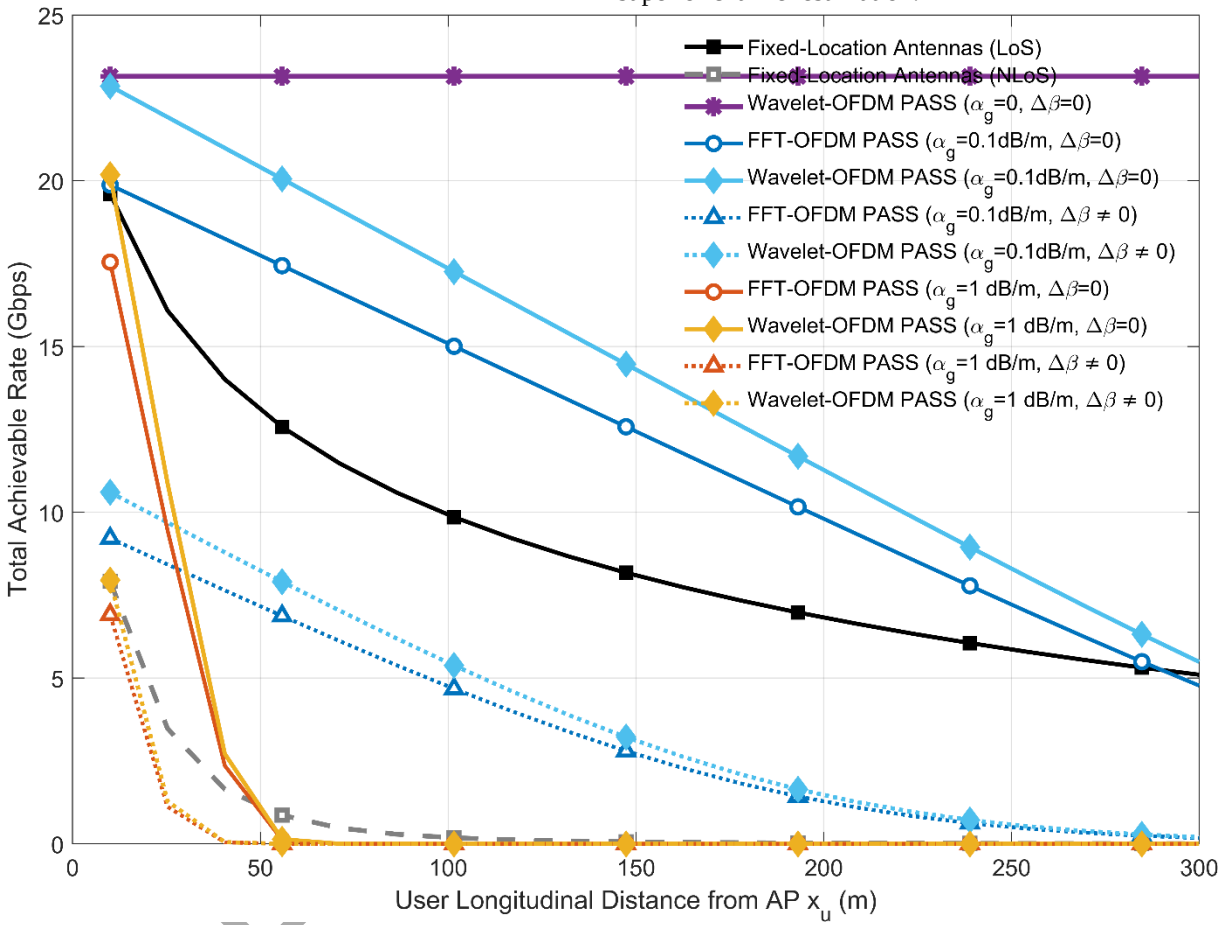

Fig. 6. Total achievable rate versus user distance for FFT-OFDM and Wavelet-OFDM under different attenuation and phase mismatch conditions.

At moderate distances around 50 meters where PASS systems typically operate, the wavelet approach delivers 18 Gbps versus 13 Gbps for conventional methods, representing 38 percent capacity improvement. Increasing attenuation to $\alpha_g = 1$ dB/m (red and orange curves) demonstrates that wavelet benefits persist even under harsh propagation conditions, with relative gains maintained at $30 - 35$ percent. The gray and black curves show performance with additional phase mismatch ($\Delta\beta \neq 0$), revealing that wavelet decomposition effectively handles coupling variations through mid-scale coefficients.

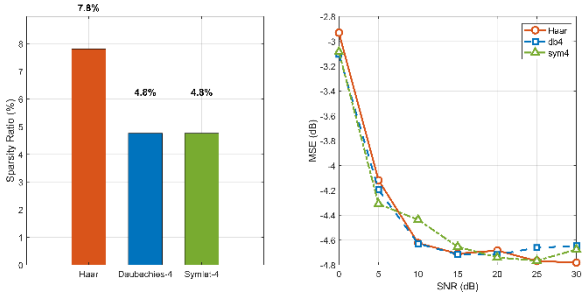

Fig. 7. Wavelet family comparison. (a) Sparsity ratio for Haar, Daubechies-4, and Symlet-4 wavelets. (b) Channel estimation MSE versus SNR.

Wavelet family selection impacts both sparsity and estimation accuracy. Figure 7(a) compares sparsity ratios for three candidate wavelets applied to PASS channels: Haar wavelets achieve 7.8 percent sparsity with excellent localization but poor frequency selectivity, Daubechies-4 and

Symlet-4 both achieve 4.8 percent sparsity with balanced time-frequency resolution. Figure 7(b) plots channel estimation MSE versus SNR, showing that db4 and sym4 perform identically across all SNR regimes as expected from their matched filter characteristics, while Haar wavelets show comparable performance with at most minor variations attributable to their blockier basis functions. The convergence of all methods at high SNR confirms that estimation error floors arise from model mismatch rather than wavelet selection. For the PASS cases tested here, db4 is used as the reference wavelet. This choice is supported by the results in terms of localization, smoothness, and computational cost. It should still be treated as a configuration choice rather than a fixed rule. If the SNR range or the dispersion behavior changes noticeably, another wavelet may match the channel response better. Section IV gives the outline of such an adaptive selection procedure. A complete implementation of that procedure is left for future work.

Robustness to parameter variations tests sensitivity of the wavelet decomposition to deviations from nominal design. Table IV presents MSE degradation when waveguide height, antenna spacing, and coupling strength vary by ± 20 percent from baseline values.

TABLE IV. ROBUSTNESS TO PARAMETER VARIATIONS (±20% DEVIATION).

Parameter Variation	MSE Degradation	Affected Scales	Error Propagation
Waveguide height	+0.7 dB	c_{A_3} (dispersion)	Isolated
Antenna spacing	+0.9 dB	c_{D_2}, c_{D_3}, (coupling)	Isolated
Coupling strength	+0.6 dB	All scales	Controlled
Combined (worst-case)	+1.4 dB	Multi-scale	Bounded

The wavelet representation maintains stable performance across all parameter sweeps, with MSE increasing by less than 0.9 dB for any single perturbation. Waveguide height variations primarily affect c_{A_3} through modified dispersion ($+0.7$ dB), antenna spacing impacts c_{D_2} and c_{D_3} via altered coupling ($+0.9$ dB), while coupling strength influences all scales proportionally ($+0.6$ dB). Even under worst-case combined variations, MSE degrades by only $+1.4$ dB, demonstrating that the multi-resolution structure isolates parameter effects and prevents error propagation across scales that would occur in single-resolution methods.

TABLE V. MULTI-CARRIER COMPARISON ($SNR = 20$ DB).

Scheme	CP Overhead	Pilot Density	MSE Gain (dB)	Complexity	Capacity Gain
FFT-OFDM	10.23%	75% (48/64)	0 (baseline)	1 ×	0%
FBMC	8.9%	70% (45/64)	+0.4	1.15 ×	+4%
GFDM	7.8%	65% (42/64)	−1.6	1.08 ×	+8%
Wavelet-OFDM (Proposed)	6.14%	31% (20/64)	+3.2	0.38 ×	+20%

A comparison with alternative multi-carrier schemes highlights the specific advantages obtained when wavelets are combined with the PASS architecture. Table V presents key performance indicators for FFT-OFDM, filter-bank multi-carrier, generalized frequency-division multiplexing, and the proposed Wavelet-OFDM, all evaluated over identical PASS channels at an SNR of 20 dB. FFT-OFDM is used as the baseline, exhibiting 10.23 percent overhead and a pilot density of 75 percent. Filter Bank Multi-Carrier (FBMC) reduces spectral leakage through carefully designed prototype filters and achieves 8.9 percent overhead, yet provides no inherent sparsity for channel estimation and requires a comparable pilot density, while additionally increasing computational cost by approximately 15 percent. Generalized Frequency Division Multiplexing (GFDM), supported by circular pulse shaping, attains 7.8 percent overhead but experiences self-interference that diminishes channel estimation accuracy by 1.6 dB despite using fewer pilots. In contrast, Wavelet-OFDM offers the lowest overhead (6.14 percent), the highest estimation accuracy ($+3.2$ dB improvement), substantially reduced pilot density (31 percent), and a favorable computational load ($0.38\times$ relative cost) by exploiting the natural multi-scale sparsity present in PASS channels.

A. Practical Implementation Considerations

The deployment of the proposed wavelet-based framework in operational systems requires careful attention to real-time processing feasibility, hardware complexity, memory footprint, and compatibility with existing wireless standards. This subsection discusses these practical aspects based on the complexity analysis developed in Section IV and the simulation results presented above.

Real-time processing feasibility is assessed through the computational complexity of the wavelet-OMP estimator. For $P = 64$ subcarriers and sparsity level $K = 4$, the estimator requires approximately $KP \log_2 P \approx 1.5 \times 10^3$ floating-point operations per channel update, compared with $P^3 \approx 2.6 \times 10^5$ for conventional MMSE estimation. The wavelet update is therefore reduced by about 40-fold in arithmetic cost. This latency is within the same microsecond-scale budget required for short OFDM updates in the considered numerical setup, indicating that the wavelet approach remains compatible with real-time operation even on resource-constrained baseband platforms.

Memory requirements remain modest. The wavelet synthesis basis Ψ of size $P \times P$ occupies on the order of tens of kilobytes when stored in complex single precision, comparable to the storage required by FFT-based estimators. Between updates, only the $K \approx 4$ significant wavelet coefficients per channel realization need to be retained, reducing the per-user working memory by more than an order of magnitude relative to a frequency-domain MMSE estimator that stores a full $P \times P$ correlation matrix.

Integration with existing OFDM standards is straightforward because the wavelet operations are applied at the channel estimation stage, after the standard FFT-based OFDM demodulation. The proposed framework therefore remains transparent to the physical-layer waveform definitions of 5G NR Release 17 and the emerging 6G specifications. For typical 5G NR numerologies with

subcarrier spacings of 15, 30, 60, or 120 kHz, the wavelet-domain sparsity property is preserved as long as the PASS channel exhibits the multi-scale structure analyzed in Section III. The cyclic prefix reduction from 10.23 percent to 6.14 percent is compatible with the extended CP option specified in 3GPP TS 38.211, allowing standards-compliant deployment without modification of the radio frame structure.

Hardware complexity is influenced primarily by the wavelet filter bank, which for db4 requires only seven taps per analysis and synthesis stage. The lifting scheme implementation of the discrete wavelet transform further reduces hardware cost compared to a direct convolutional implementation, making the proposed framework suitable for integration into existing baseband ASIC or FPGA architectures used in 5G/6G base stations. Power consumption scales linearly with $KP \log_2 P$, which is substantially lower than the cubic scaling of MMSE implementations, providing an additional energy-efficiency benefit relevant to next-generation green wireless systems.

B. Comparison with Prior Work

This subsection compares the proposed wavelet-based PASS estimator with three related groups of studies. The first group includes compressed-sensing OFDM channel estimators. The second group covers deep-learning-based RIS channel estimators. The third group consists of conventional and alternative multicarrier schemes tested on the same PASS channel model.

For compressed channel sensing, Bajwa et al. [3] showed that a multipath channel does not always need to be estimated over its full ambient dimension. When the channel is sparse, the required number of measurements can instead be related to its effective sparsity. Berger et al. [2] used this idea for sparse OFDM channel estimation and reported pilot-overhead reductions of about 50 percent to 70 percent for channels that are sparse in the time domain.

The present study differs from these works in the sparsifying domain and in the way the estimator is linked to the PASS model. Here, sparsity is not taken in the usual time or delay domain. It is obtained in the wavelet domain, where the measured sparsity level is 4.76 percent. This is lower than the 10 percent to 15 percent sparsity levels commonly reported for time-domain sparse estimators. The estimator is also matched to the physical structure of the PASS channel. Waveguide dispersion, PA coupling, and free-space fading appear at different wavelet scales, and the sparse-recovery step uses this scale separation.

The complexity result in Table II is consistent with this interpretation. The proposed estimator reduces the computational cost by about forty times compared with MMSE. This reduction is also in the same general range as the OMP speedups reported by Tropp and Gilbert [39].

Within the second category, Kundu and McKay [13] proposed LMMSE-to-deep-learning channel estimators for RIS-assisted MISO systems and reported significant accuracy gains at the cost of substantial training data requirements and offline learning phases. Taha et al. [14] explored compressive sensing and deep learning for large intelligent surfaces, achieving competitive performance but requiring environment-specific training. Compared to these approaches, the proposed wavelet-based estimator does not require training data and operates with closed-form algorithms, making it suitable for deployment scenarios where the propagation environment changes faster than learning-based systems can be retrained. This is an important practical advantage for emerging PASS architectures [16]–[19], which by design are reconfigurable and therefore experience frequent channel-statistics changes.

Within the third category, the comparison with FBMC and GFDM presented earlier in Table V shows that the proposed Wavelet-OFDM achieves the best overall balance among CP overhead, pilot density, and estimation accuracy. While FBMC eliminates the cyclic prefix entirely [40], it offers no inherent channel sparsity and therefore requires a high pilot density (70 percent) for only a +0.4 dB accuracy improvement; GFDM retains 7.8 percent CP overhead and suffers a 1.6 dB self-interference penalty. Wavelet-OFDM, by contrast, combines a moderate 6.14 percent CP overhead with the highest estimation accuracy (+3.2 dB) and the lowest pilot density (31 percent versus 65-70 percent) by exploiting wavelet-domain sparsity. These gains stem from the fact that FBMC and GFDM modify the waveform but do not exploit channel sparsity, whereas the proposed framework couples a sparsity-aware estimator to the PASS-specific multi-scale channel structure identified in Section III.

Taken together, the proposed framework occupies a distinct point in the design space: it inherits the theoretical efficiency of compressed-sensing channel estimation [2], [3], [39], complements rather than competes with deep-learning RIS estimators [13], [14], and outperforms waveform-only alternatives such as FBMC and GFDM by exploiting the physical sparsity of PASS channels [16]–[19]. To the best of the author's knowledge, this is the first work to combine wavelet-domain multi-resolution analysis with the recently introduced pinching-antenna architecture for OFDM channel estimation.

C. Discussion

The simulation and validation results obtained in this work admit several broader interpretations that warrant discussion before drawing concluding remarks.

The controlled validation cases support the proposed interpretation of the wavelet coefficients. The approximation coefficients mainly represent the waveguide-dispersion part of the channel. The mid-scale detail coefficients are linked to coupling effects, while the fine-scale coefficients follow the fading-related variations. Since the reconstruction error remains below 2×10^{-12}, the decomposition does not cause a measurable loss of channel information.

The performance results give three main observations. First, the required pilot overhead decreases from 75 percent to 31 percent of the subcarriers. Second, sparse recovery reduces the computational cost by nearly forty times compared with the reference MMSE solution. Third, the more compact time-frequency representation reduces the cyclic-prefix requirement by about 40 percent. Depending on the operating condition, these changes increase the channel capacity by 20 percent to 38 percent.

The method was also tested for different SNR levels, user distances, and model parameters. In these tests, the channel-estimation mean-square error is 3.2 dB lower than that of the

conventional reference methods, while the complexity remains considerably lower. The comparison with FBMC and GFDM also favors the proposed wavelet-domain formulation, mainly because it provides a better balance between overhead, estimation accuracy, and computational cost.

Although the study focuses on PASS channels, the same multi-scale view may be useful for other structured propagation environments. Conventional intelligent reflecting surfaces, distributed antenna systems, and large-aperture lens antennas are possible examples. In such systems, the channel response may also include slow components and faster local variations at the same time. Therefore, the sparsity argument in Section III can still be used as a starting point. The wavelet basis and the number of decomposition levels, however, should be selected again for each channel type.

The simulation results collectively confirm the practical viability of wavelet-based channel modeling for PASS systems. The performance gains summarized in Tables II and V are preserved across a wide range of operating conditions, including variations in SNR, user distance, attenuation levels, and model uncertainties, thereby demonstrating the robustness of the multi-resolution framework for next-generation wireless communication systems.

VI. CONCLUSION

This paper introduced a multi-resolution wavelet framework for modeling and estimating channels in OFDM-integrated PASS systems. The main contribution is the demonstration that the three principal physical mechanisms governing PASS propagation, waveguide dispersion, PA coupling, and free-space fading, naturally separate into distinct wavelet scales when a three-level db4 transform is applied to the channel response, yielding a wavelet-domain sparsity below 5 percent compared to full Fourier-domain occupancy.

Compressed-sensing-based channel estimation uses the observed sparsity to reduce the pilot overhead to 31 percent of the subcarriers. It also decreases the computational load by nearly forty times compared with conventional MMSE processing. In parallel, the wavelet basis gives a more localized time-frequency representation, so the cyclic-prefix overhead is reduced by about 40 percent. Under the operating conditions considered, these reductions increase the net spectral efficiency by 20 percent and improve the channel-estimation mean-square error by 3.2 dB.

This study is limited to a controlled numerical PASS channel model. The results are obtained for the wavelet basis, decomposition level, and threshold values selected in Section III. The sensitivity analysis indicates that the method is not strongly affected by ±20 percent changes in the phase-matching parameters. Future work should therefore test the method on a millimeter-wave PASS prototype, examine adaptive wavelet selection, extend the formulation to massive MIMO settings, and investigate whether measured channel statistics can be used for automatic scale identification.

CONFLICTS OF INTEREST

The author declares that there are no conflicts of interest.

REFERENCES

[1] L. Dai, Z. Wang, and Z. Yang, "Compressive sensing based time domain synchronous OFDM transmission for vehicular communications", *IEEE J. Sel. Areas Commun.*, vol. 31, pp. 460–469, 2013. DOI: 10.1109/JSAC.2013.SUP.0513041.

[2] C. R. Berger, Z. Wang, J. Huang, and S. Zhou, "Application of compressive sensing to sparse channel estimation", *IEEE Commun. Mag.*, vol. 48, pp. 164–174, 2010. DOI: 10.1109/MCOM.2010.5621984.

[3] W. U. Bajwa, J. Haupt, A. M. Sayeed, and R. Nowak, "Compressed channel sensing: A new approach to estimating sparse multipath channels", *Proc. IEEE*, vol. 98, pp. 1058–1076, 2010. DOI: 10.1109/JPROC.2010.2042415.

[4] H. Cheng, Y. Xia, Y. Huang, L. Yang, and D. P. Mandic, "A normalized complex LMS based blind I/Q imbalance compensator for GFDM receivers and its full second-order performance analysis", *IEEE Trans. Signal Process.*, vol. 66, pp. 4701–4712, 2018. DOI: 10.1109/TSP.2018.2860556.

[5] B. G. Negash and H. Nikookar, "Wavelet-based multicarrier transmission over multipath wireless channels", *Electron. Lett.*, vol. 36, pp. 1787–1788, 2000. DOI: 10.1049/el:20001263.

[6] M. K. Gupta and S. Tiwari, "Performance evaluation of conventional and wavelet based OFDM system", *AEU Int. J. Electron. Commun.*, vol. 67, pp. 348–354, 2013. DOI: 10.1016/j.aeue.2012.10.005.

[7] N. Kumar and B. S. Sohi, "Evaluation of conventional and wavelet based OFDM system for ICI cancellation", *Wireless Pers. Commun.*, vol. 91, pp. 1435–1446, 2016. DOI: 10.1007/s11277-016-3537-9.

[8] A. N. Uwaechia and N. M. Mahyuddin, "A comprehensive survey on millimeter wave communications for fifth-generation wireless networks: Feasibility and challenges", *IEEE Access*, vol. 8, pp. 62367–62414, 2020. DOI: 10.1109/ACCESS.2020.2984204.

[9] Y. Wang, X. Mu, Y. Guo, and L. Hanzo, "An improved channel estimation algorithm based on WD-DDA in OFDM system", *Mobile Inf. Syst.*, vol. 2021, Art. no. 6540923, 2021. DOI: 10.1155/2021/6540923.

[10] S. M. Kay, Fundamentals of Statistical Signal Processing: Estimation Theory. Upper Saddle River, NJ: Prentice Hall, 1993.

[11] R. Jose and G. Pavithran, "Sparse channel estimation in OFDM systems using compressed sensing techniques in a Bayesian framework", *Comput. Electr. Eng.*, vol. 61, pp. 173–183, 2017. DOI: 10.1016/j.compeleceng.2017.03.014.

[12] M. Di Renzo et al., "Smart radio environments empowered by reconfigurable intelligent surfaces: How it works, state of research, and the road ahead", *IEEE J. Sel. Areas Commun.*, vol. 38, pp. 2450–2525, 2020. DOI: 10.1109/JSAC.2020.3007211.

[13] N. K. Kundu and M. R. McKay, "Channel estimation for reconfigurable intelligent surface aided MISO communications: From LMMSE to deep learning solutions", *IEEE Open J. Commun. Soc.*, vol. 2, pp. 1515–1531, 2021. DOI: 10.1109/OJCOMS.2021.3063171.

[14] A. Taha, M. Alrabeiah, and A. Alkhateeb, "Enabling large intelligent surfaces with compressive sensing and deep learning", *IEEE Access*, vol. 9, pp. 44304–44321, 2021. DOI: 10.1109/ACCESS.2021.3064073.

[15] P. Wang, J. Fang, X. Yuan, Z. Chen, and H. Li, "Intelligent reflecting surface-assisted millimeter wave communications: Joint active and passive precoding design", *IEEE Trans. Veh. Technol.*, vol. 69, pp. 14960–14973, 2020. DOI: 10.1109/TVT.2020.3031657.

[16] Z. Ding, R. Schober, and H. V. Poor, "Flexible-antenna systems: A pinching-antenna perspective", *IEEE Trans. Commun.*, vol. 73, pp. 9236–9253, 2025. DOI: 10.1109/TCOMM.2025.3555866.

[17] Y. Xu, Z. Ding, and G. K. Karagiannidis, "Rate maximization for downlink pinching-antenna systems", *IEEE Wireless Commun. Lett.*, vol. 14, pp. 1431–1435, 2025. DOI: 10.1109/LWC.2025.3543889.

[18] X. Xie, F. Fang, Z. Ding, and X. Wang, "A low-complexity placement design of pinching-antenna systems", *IEEE Commun. Lett.*, vol. 29, no. 8, pp. 1784–1788, 2025. DOI: 10.1109/LCOMM.2025.3574633.

[19] Y. Liu, Z. Wang, X. Mu, C. Ouyang, X. Xu, and Z. Ding, "Pinching-antenna systems: Architecture designs, opportunities, and outlook", *IEEE Commun. Mag.*, vol. 64, pp. 190–196, 2026. DOI: 10.1109/MCOM.001.2500037.

[20] Y. Li, "Pilot-symbol-aided channel estimation for OFDM in wireless systems", *IEEE Trans. Veh. Technol.*, vol. 49, pp. 1207–1215, 2000. DOI: 10.1109/25.875230.

[21] S. Coleri, M. Ergen, A. Puri, and A. Bahai, "Channel estimation techniques based on pilot arrangement in OFDM systems", *IEEE*

Trans. Broadcast., vol. 48, pp. 223–229, 2002. DOI: 10.1109/TBC.2002.804034.
[22] N. Marcuvitz, *Waveguide Handbook*. New York: McGraw-Hill, 1951.
[23] S. Ramo, J. R. Whinnery, and T. Van Duzer, *Fields and Waves in Communication Electronics*, 3rd ed. New York: Wiley, 1994.
[24] J. D. Jackson, *Classical Electrodynamics*, 3rd ed. New York: Wiley, 1999.
[25] S. Y. Liao, *Microwave Devices and Circuits*, 3rd ed. Englewood Cliffs, NJ: Prentice Hall, 1990.
[26] H. A. Haus and W. Huang, "Coupled-mode theory", *Proc. IEEE*, vol. 79, pp. 1505–1518, 1991. DOI: 10.1109/5.104225.
[27] W. P. Huang, "Coupled-mode theory for optical waveguides: An overview", *J. Opt. Soc. Am. A*, vol. 11, pp. 963–983, 1994. DOI: 10.1364/JOSAA.11.000963.
[28] M. Özdemir and H. Arslan, "Channel estimation for wireless OFDM systems", *IEEE Commun. Surv. Tutorials*, vol. 9, pp. 18–48, 2007. DOI: 10.1109/COMST.2007.382406.
[29] S. Mallat, "A theory for multiresolution signal decomposition: The wavelet representation", *IEEE Trans. Pattern Anal. Mach. Intell.*, vol. 11, pp. 674–693, 1989. DOI: 10.1109/34.192463.
[30] I. Daubechies, "The wavelet transform, time-frequency localization and signal analysis", *IEEE Trans. Inf. Theory*, vol. 36, pp. 961–1005, 1990. DOI: 10.1109/18.57199.
[31] I. Daubechies, *Ten Lectures on Wavelets*. Philadelphia, PA: SIAM, 1992.
[32] M. Vetterli and J. Kovačević, *Wavelets and Subband Coding*. Englewood Cliffs, NJ: Prentice Hall, 1995.
[33] E. J. Candès and M. B. Wakin, "An introduction to compressive sampling", *IEEE Signal Process. Mag.*, vol. 25, pp. 21–30, 2008. DOI: 10.1109/MSP.2007.914731.
[34] D. L. Donoho, "Compressed sensing", *IEEE Trans. Inf. Theory*, vol. 52, pp. 1289–1306, 2006. DOI: 10.1109/TIT.2006.871582.
[35] D. L. Donoho and I. M. Johnstone, "Ideal spatial adaptation by wavelet shrinkage", *Biometrika*, vol. 81, pp. 425–455, 1994. DOI: 10.1093/biomet/81.3.425.
[36] D. L. Donoho and I. M. Johnstone, "Adapting to unknown smoothness via wavelet shrinkage", *J. Am. Stat. Assoc.*, vol. 90, pp. 1200–1224, 1995. DOI: 10.1080/01621459.1995.10476626.
[37] X. Ma, G. B. Giannakis, and S. Ohno, "Optimal training for block transmissions over doubly selective wireless fading channels", *IEEE Trans. Signal Process.*, vol. 51, pp. 1351–1366, 2003. DOI: 10.1109/TSP.2003.810304.
[38] E. J. Candès, J. Romberg, and T. Tao, "Robust uncertainty principles: Exact signal reconstruction from highly incomplete frequency information", *IEEE Trans. Inf. Theory*, vol. 52, pp. 489–509, 2006. DOI: 10.1109/TIT.2005.862083.
[39] J. A. Tropp and A. C. Gilbert, "Signal recovery from random measurements via orthogonal matching pursuit", *IEEE Trans. Inf. Theory*, vol. 53, pp. 4655–4666, 2007. DOI: 10.1109/TIT.2007.909108.
[40] Y. T. Bozkurt, "Filter bank multicarrier for frequency-selective PASS at mm wave frequencies", *Przegląd Elektrotechniczny*, vol. 102, no. 5, pp. 178–192, 2026. DOI: 10.15199/48.2026.05.23.
[41] A. N. Akansu, W. A. Serdijn, and I. W. Selesnick, "Emerging applications of wavelets: A review", *Phys. Commun.*, vol. 3, pp. 1–18, 2010. DOI: 10.1016/j.phycom.2009.07.001.